Influence of atmospheric rivers on the Leeuwin Current system

Toshiaki Shinoda, Weiqing Han, Luis Zamudio & Xue Feng

Climate Dynamics

Observational, Theoretical and Computational Research on the Climate System

ISSN 0930-7575 Volume 54 Combined 9-10

Clim Dyn (2020) 54:4263-4277 DOI 10.1007/s00382-020-05228-z



Your article is protected by copyright and all rights are held exclusively by Springer-Verlag GmbH Germany, part of Springer Nature. This e-offprint is for personal use only and shall not be self-archived in electronic repositories. If you wish to self-archive your article, please use the accepted manuscript version for posting on your own website. You may further deposit the accepted manuscript version in any repository, provided it is only made publicly available 12 months after official publication or later and provided acknowledgement is given to the original source of publication and a link is inserted to the published article on Springer's website. The link must be accompanied by the following text: "The final publication is available at link.springer.com".





Influence of atmospheric rivers on the Leeuwin Current system

Toshiaki Shinoda¹ · Weiqing Han² · Luis Zamudio³ · Xue Feng¹

Received: 4 September 2019 / Accepted: 1 April 2020 / Published online: 20 April 2020 © Springer-Verlag GmbH Germany, part of Springer Nature 2020

Abstract

Previous work has demonstrated the strong ocean response to atmospheric rivers (ARs) in the northeast Pacific including coastal currents along the west coast of North America, because of strong surface winds associated with ARs. A recent study on the global distribution of ARs also suggests that the southeast Indian Ocean is one of the areas of relatively strong AR activity. This study investigates the influence of ARs on the Leeuwin Current system, which is one of the major boundary currents in the Indian Ocean. It is demonstrated that winds associated with typical ARs in the southeast Indian Ocean can generate strong poleward coastal currents and sea level rise along the west coast of Australia using a high-resolution ocean reanalysis (0.08° HYCOM). The composite of upper ocean currents and sea surface height (SSH) associated with landfalling ARs along the west coast of Australia is constructed using the HYCOM reanalysis, long-term AR data set, and tide gauge data. The enhancement of the poleward currents generated by ARs is found in the composite, and the magnitude of the enhancement is comparable to the strength of the Leeuwin Current itself. The results also indicate that the fluctuation of SSH and coastal currents along the west coast propagates along the southern coast all the way to the southeast coast (Pacific side) of Australia. The SSH propagation along the coasts is also detected in the tide gauge data in the west and southern coasts of Australia.

1 Introduction

Atmospheric rivers (ARs) are narrow and relatively long regions of concentrated moisture in the atmosphere which transport a substantial amount of water vapor from the (sub) tropics to the mid-latitude (Zhu and Newell 1998; Newell and Zhu 1994; Ralph et al. 2004). When ARs make landfall, they can cause extreme rainfall and floods in many locations especially along the west coasts of mid-latitude continents (e.g., Western North America, Northern Europe). Because of such significant societal impacts including flooding in highly populated regions, atmospheric processes associated with landfalling ARs in the northeast Pacific and western Europe are extensively studied in the last few decades (e.g., Ralph et al. 2006; Bao et al. 2006; Neiman et al. 2008; Guan et al. 2010, 2013; Dettinger 2011; Doyle et al. 2014; Kim et al. 2017; Reynolds et al. 2019 and many others).

☐ Toshiaki Shinoda toshiaki.shinoda@tamucc.edu

In addition to the extreme rainfall produced by landfalling ARs, a recent study emphasizes the extreme wind events associated with ARs (Waliser and Guan 2017). Using a global AR data set, Waliser and Guan (2017) demonstrate that ARs are associated with up to half of extreme wind events (top 2% of wind distribution) in most mid-latitude regions. These include many landfalling ARs, which can cause a doubling or more of the typical surface wind speed compared to all storm conditions and a substantial (50–100%) increase of wind speed for extreme events over the coastlines.

Given such rapid changes in winds associated with ARs, it is expected that AR-induced winds can generate large fluctuations of upper ocean structure including strong currents. A recent study demonstrates the strong ocean response to ARs in the northeast Pacific, which includes strong coastal jets along the west coast of North America (Shinoda et al. 2019). Because the direction of surface currents generated by AR-associated winds is nearly perpendicular to the north American coastline, ARs also generate prominent sea level rise over the broad areas along the west coast of north America.

While many previous studies focus on the landfalling ARs around the west coast of north America and Europe (e.g.



Texas A&M University - Corpus Christi, Corpus Christi, TX 78412, USA

² University of Colorado, Boulder, USA

Florida State University, Tallahassee, USA

Reynolds et al. 2019; Doyle et al. 2014; Kim and Alexander 2015), some of the recent studies demonstrate that strong ARs are observed in many other areas including those in the southern hemisphere and the western portion of ocean basins (Guan and Waliser 2015; Mundhenk et al. 2016; Hirota et al. 2016). A global distribution of ARs suggests that the southeast Indian Ocean is one of the areas of relatively strong AR activity. Strong ARs often make landfall along the west coast of Australia where the frequency of the landfalling exceeds 16 days/year (Guan and Waliser 2015). Figure 1 shows a few examples of landfalling AR events in the southeast Indian Ocean. The spatial pattern of moisture

transport and its relation to the land are similar to those in the northeast Pacific, except the direction of moisture flux is southeastward. While these ARs may not generate extreme rainfall events and flooding because of the lack of high mountain areas around the west coast of Australia, AR-associated strong winds are likely to generate prominent upper ocean response such as that observed along the west coast of north America.

Ocean circulations in the southeast Indian Ocean are complex and unique compared to those in the eastern portion of other ocean basins. For example, unlike most eastern boundary currents in other ocean basins, the Leeuwin Current (LC),

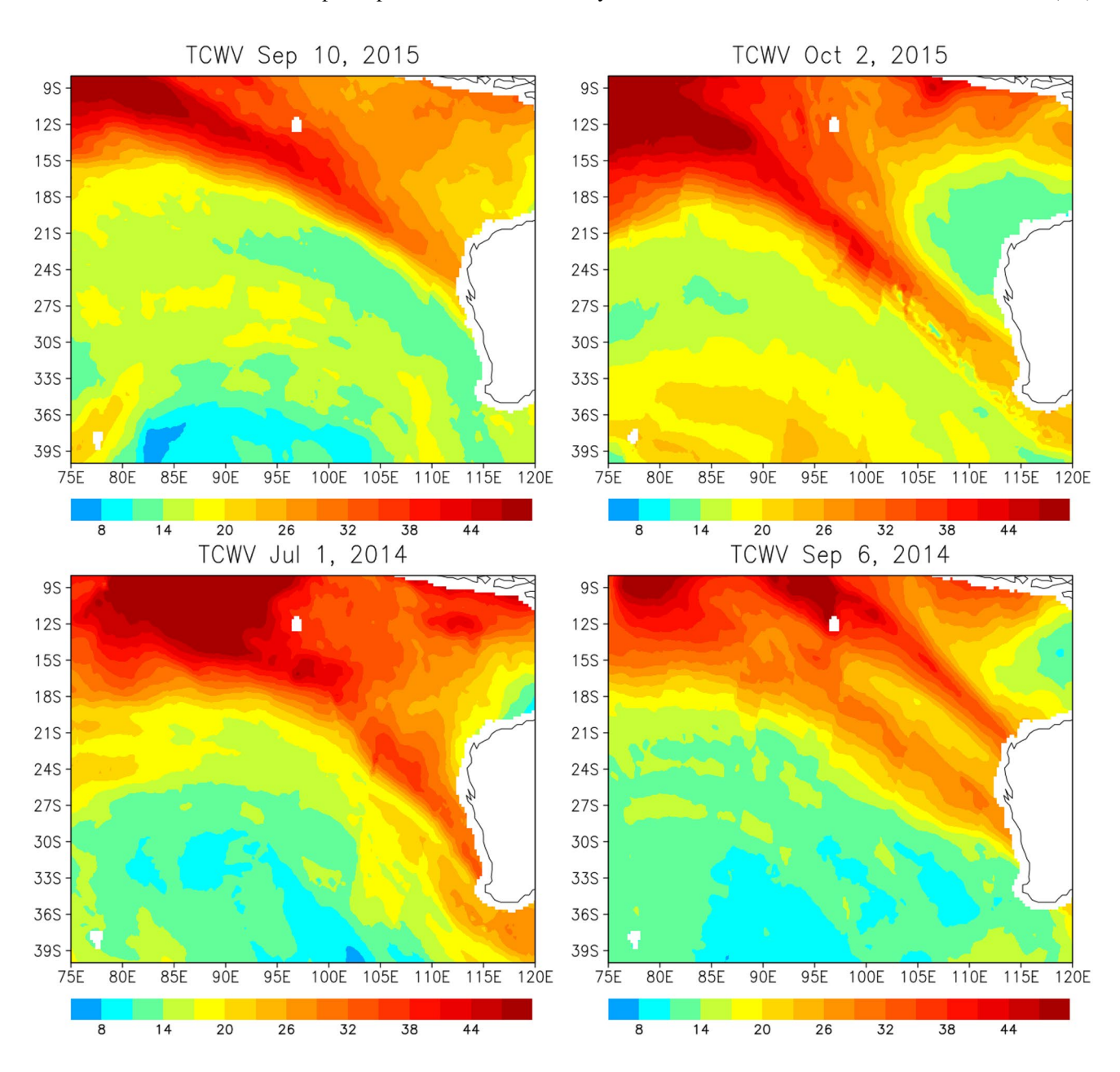


Fig. 1 Total column integrated water vapor (mm) on September 10, 2015 (upper left panel), October 2, 2015 (upper right panel), July 1, 2014 (bottom left panel), and September 6, 2014 (bottom right panel) derived from SSMI data



which is one of the major boundary currents in the Indian Ocean, flows poleward against the prevailing equatorward surface winds (e.g., Cresswell and Golding 1980; Church et al. 1989). The annual mean velocity of the LC is about 0.3 m/s (e.g., Feng et al. 2003), which carries warm waters from the tropics to midlatitude and could largely influence SSTs near the west coast of Australia. Hence it has a strong impact on the regional climate in the southeast Indian Ocean on a variety of time scales. For example, previous studies indicate that the Leeuwin Current plays an important role in the onset of Ningaloo Niño, which is one of the major interannual climate variability in the Indian Ocean and is associated with an ocean warming and heat wave off the west coast of Australia (Feng et al. 2013). Recent studies suggest that the Ningaloo Niño influences climate variability outside of the Indian Ocean through changes in large-scale atmospheric circulations (e.g., Zhang and Han 2018). For example, Zhang and Han (2018) suggest that anomalous SSTs associated with the Ningaloo Niño in the southeast Indian Ocean can cause the enhancement of trade winds in the western Pacific and the upper ocean cooling in the central Pacific through the atmospheric teleconnection. Accordingly, it is crucial to improve our understanding of ocean circulation variability in the southeast Indian Ocean especially the LC.

Despite the importance of the LC on regional and global climate variability, its accurate simulations by large-scale ocean and climate models are still a major challenge partly because it requires to resolve the narrow width of the current which is only about 30-50 km. Hence it has been difficult to examine how the LC system is influenced by atmospheric disturbances such as those produced by ARs until recently due primarily to the lack of high-resolution ocean data which covers both open ocean and coastal areas. Because of the recent development of high-resolution ocean reanalysis (Metzger et al. 2014), it is now feasible to examine the variability of a narrow coastal current and its relation to open ocean variability produced by large-scale atmospheric forcing generated by ARs (Shinoda et al. 2019). This study investigates the upper ocean response to ARs in the southeast Indian Ocean including the LC system using a high-resolution ocean reanalysis. The available tide-gauge data along the west and southern coasts of Australia are also used to validate the results obtained from the analysis of the ocean reanalysis. A particular emphasis is given to the generation of coastal currents by AR-associated winds and propagation of sea level and alongshore currents fluctuations along the west and southern coasts of Australia.

2 Data

2.1 Ocean reanalysis

The high-resolution global ocean reanalysis data set, created by the US Navy's operational Global Ocean Now-cast/Forecast System (Metzger et al. 2014), is used in this study. The system employs the 0.08° Hybrid Coordinate Ocean Model (HYCOM; Bleck 2002) as an ocean model component, and in-situ and satellite data are assimilated through the Navy Coupled Ocean Data Assimilation (NCODA; Commings et al. 2013). This reanalysis product is referred to as "HYCOM reanalysis" hereafter.

HYCOM, NCODA and the data assimilation method are explained here briefly, as the details are described in other papers (Bleck 2002; Commings et al. 2013; Metzger et al. 2014; Helber et al. 2013). The global HYCOM used in this study is eddy-resolving, with the horizontal resolution of 0.08° at the equator. The HYCOM is driven by surface forcing fields derived from the Climate Forecast System Reanalysis products (CFSR; Saha et al. 2010). The ocean data assimilated by NCODA include remotely-sensed sea surface height (SSH), sea surface temperature (SST) and sea ice concentration plus in situ surface and subsurface temperature and salinity observations. The latest version of HYCOM/NCODA system uses synthetic temperature profiles derived from the Improved Synthetic Ocean Profile (ISOP; Helber et al. 2013). The ISOP is constructed at a given location by projecting satellite-derived SSH and SST downward from the surface using statistical relationships for the global domain. It should be noted that the subsurface temperature profiles are significantly improved by using ISOP, compared to the previous version of the HYCOM reanalysis in which the Modular Ocean Data Assimilation System (MODAS) is employed.

Although the HYCOM ocean reanalysis covers for the period of 1993–2015, surface forcing fields used for the product have been changed from CFSRV1 to Climate Forecast System Version 2 (CFSV2) from 2011, with the accompanying increase of horizontal resolution from 0.3125° to 0.205°. In this study, the daily mean ocean velocity and SSH data for the period of 2011–2015 are used. It should be noted that the analysis period of 5 years is long enough for the present study, as many AR events are identified in the southeast Indian Ocean during the 5-year period of 2011–2015.

In the last several years, the HYCOM reanalysis has been validated extensively, including the ocean variability associated with ARs (e.g., Shinoda et al. 2019; Yu et al. 2015; Thopil et al. 2016). In particular, the 0.08° HYCOM is able to resolve upper ocean variability near the boundary including the narrow boundary currents, which cannot



be well monitored by satellite observations only. It should be noted that the satellite altimeter data are not able to well resolve the sea-level change produced by ARs discussed in this study based on our preliminary analysis.

To further evaluate the HYCOM reanalysis in the southeast Indian Ocean, the structure of the LC in the reanalysis is compared with observations. Figure 2 shows the meridional currents along 32°S where the observational structure of the LC has been reported in several previous studies (e.g., Feng et al. 2003, Furue et al. 2017). The LC has a remarkable seasonal variation, which is strong in the austral fall/winter seasons with the maximum poleward transport being observed during June-July (Feng et al. 2003). Here the LC structure during May-August when the LC is relatively strong is compared. The realistic LC is shown to be reproduced in the HYCOM reanalysis. The strength, horizontal and vertical structures of the LC are all consistent with the previous studies of observations in this region (e.g., Fig. 7 in Feng et al. 2003). For example, the LC core with the velocity of about 30-40 cm/s is located around 115°E in both observations and the HYCOM reanalysis.

2.2 Tide gauge and surface wind data

Sea level data derived from tide gauges at four stations, Fremantle, Esperance, Thevenard, and Portland located along the west and southern coasts of Australia are used to investigate sea level fluctuations associated with ARs. The tide gauge data are provided at the University of Hawaii Sea Level Center. To describe surface wind fields associated with ARs, daily mean winds at 10 m derived from CFSV2 are analyzed, which have been used for creating the HYCOM reanalysis.

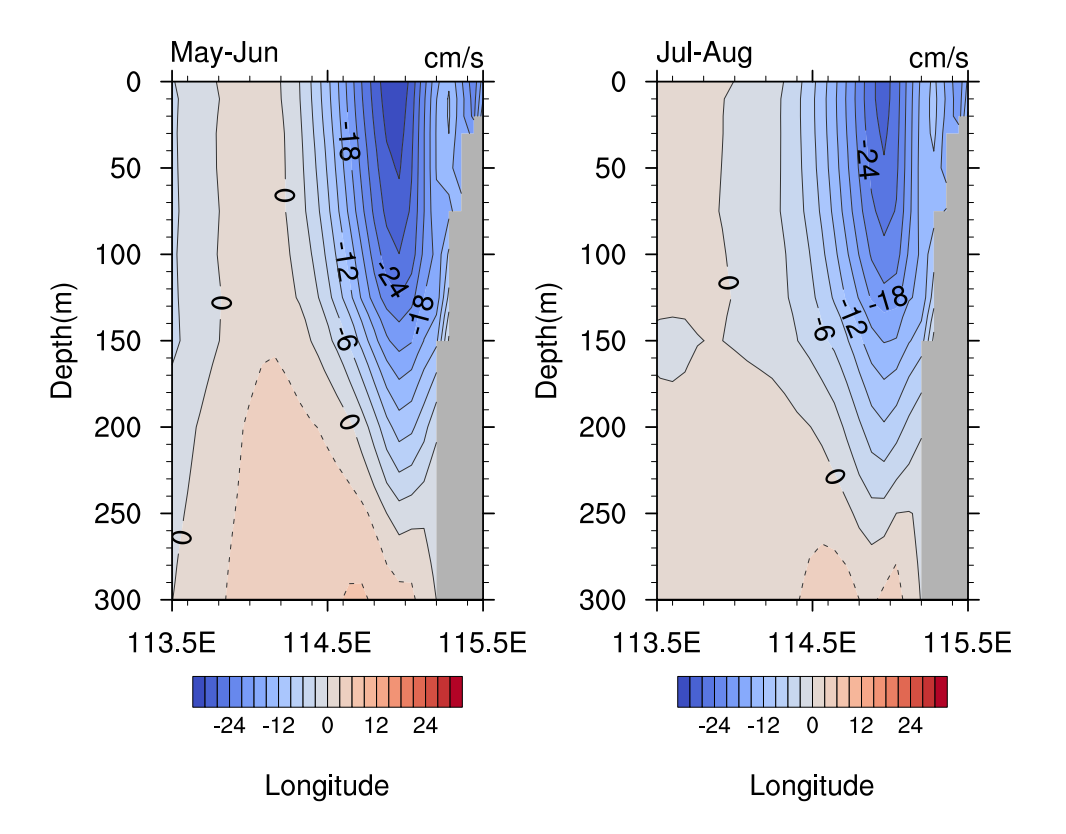
3 Results

3.1 Ocean response to individual AR event: case study

Ocean response to individual AR events shown in Fig. 1 is first investigated. Here, the results for the event in early September (upper left panel in Fig. 1) are discussed. It should be noted that major features of ocean variability found in the September event are evident in all other three AR events shown in Fig. 1 (not shown).

Figure 3 shows the time evolution of total column integrated water vapor (TCWV) when the AR made landfall. Landfalling occurred around September 9 when the region of high moisture concentration reached a southern part of the west coast of Australia. In association with the eastward movement of the high moisture area, strong northwesterlies associated with cyclonic circulations moved eastward and reached the coast when the AR made landfall (Fig. 4, left panels). The surface winds exceed 12 m/s in the large areas of the cyclonic circulation, and the maximum winds of about

Fig. 2 Climatological mean meridional velocity along 32°S during May–June (left panel) and July–August (right panel) from the HYCOM reanalysis





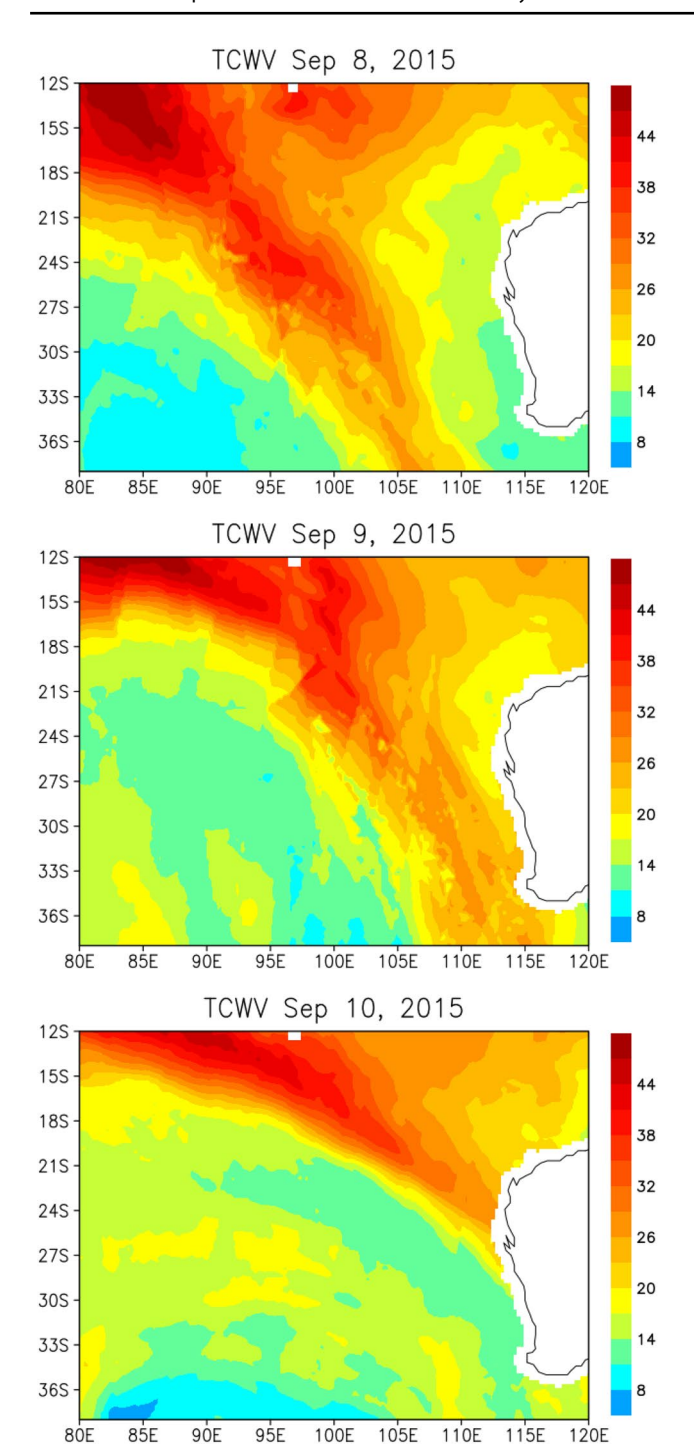


Fig. 3 Total column integrated water vapor (mm) on September 8 (upper panel), September 9 (middle panel), and September 10 (bottom panel), 2015 derived from SSMI data

20 m/s are found on September 10. The relation between the high moisture areas and strong winds are similar to that for the events in the northeast Pacific (Shinoda et al. 2019). The strongest winds are found in the area of high moisture concentration, which is located between the cyclonic and anticyclonic circulations. The presence of the anticyclone

located northeast side of the cyclone is an essential component of AR system, resulting in large horizontal pressure gradients between the cyclone and anticyclone, and thus a relatively narrow band of strong winds (Guo et al. 2020).

Surface ocean current fields in this region are noisy because of the active mesoscale and sub-mesoscale eddies (Fig. 4 right panels), consistent with previous observational and modeling studies (e.g., Andrews 1977; Pearce and Griffiths 1991; Batteen et al. 1992; Feng et al. 2005). Yet the enhancement of eastward currents induced by strong northwesterlies are evident in Fig. 4. For example, on September 8, eastward and southeastward currents associated with northwesterlies are found around 102° E-105° E, 32° S-34° S. This current pattern moved eastward with the atmospheric disturbance and reached near the coast on September 9, in which strong southward along-shore currents along the west coast, that are connected to the eastward (on-shore) currents, are generated. The acceleration of the eastward and alongshore currents are found more clearly in the surface current difference between September 8 and September 9 when the AR made landfall (Fig. 5). The increase of southward current speeds exceeds 0.3 m/s, which is comparable to the strength of the mean LC itself. The vertical structure of the acceleration of the southward currents is shown in Fig. 6, in which the enhancement extends all the way to the bottom (100–120 m depths) in the shelf break region. Note that the zonal currents along the same section reveal that the strong eastward currents around 110° E-113° E (Fig. 5) are mostly confined within the upper 30 m (not shown), which is consistent with the direct response to the northwesterly winds.

Figure 7a shows the time series of daily mean sea level from the tide gauge at Fremantle during the AR event discussed above. The rapid sea level rise is clearly evident during the AR landfall on September 8-9, which is consistent with previous studies that demonstrate the close relationship between the sea level at Fremantle and the strength of the LC (e.g., Feng et al. 2003). Such rapid sea level rise is also found in the HYCOM reanalysis (Fig. 7b). The magnitude of the sea level rise observed by the tide gauge during this period exceeds 20 cm. The magnitude in the HYCOM reanalysis is comparable, but a slightly smaller partly because it is the model grid scale average. Nevertheless, a good agreement of sea level variability during the AR event suggests that the large acceleration of southward currents associated with sea level rise caused by AR-associated winds found in the HYCOM reanalysis is realistic.

The ocean response to the AR event described above is similar to that in the northeast Pacific. As shown in Fig. 4, the AR system consists of a cyclone and an anticyclone located on the eastern equatorward of the cyclone; the strong winds and high moisture concentration are found between the cyclone and anticyclone where strong horizontal pressure gradients are located. The strong



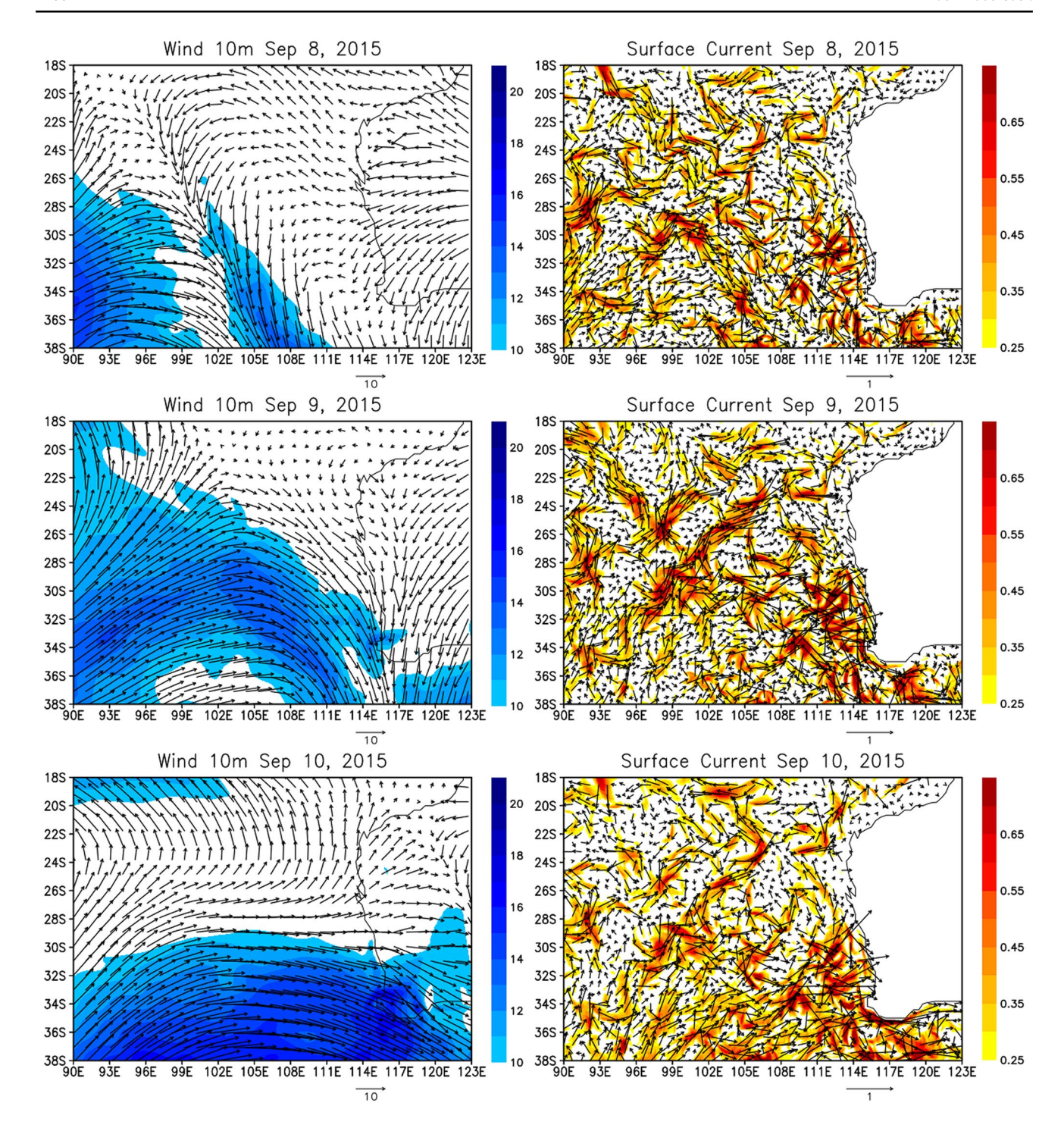


Fig. 4 Left panels: Winds at 10 m height on September 8 (upper panel), September 9 (middle panel), and September 10 (lower panel), 2015 from CFSV2 analysis. Shading indicates wind speed (m/s).

Right panels: surface currents on September 8 (upper panel), September 9 (middle panel), and September 10 (lower panel), 2015 from HYCOM reanalysis. Shading indicates current speed (m/s)

northwesterly winds generate eastward surface currents whose direction is nearly perpendicular to the coastline. Hence the AR-associated winds can effectively generate rapid sea level rise, which is associated with strong southward currents along the coast.

3.2 Composite evolution of upper ocean currents and sea level

To examine whether major features in ocean variability associated with the AR event described above are representative



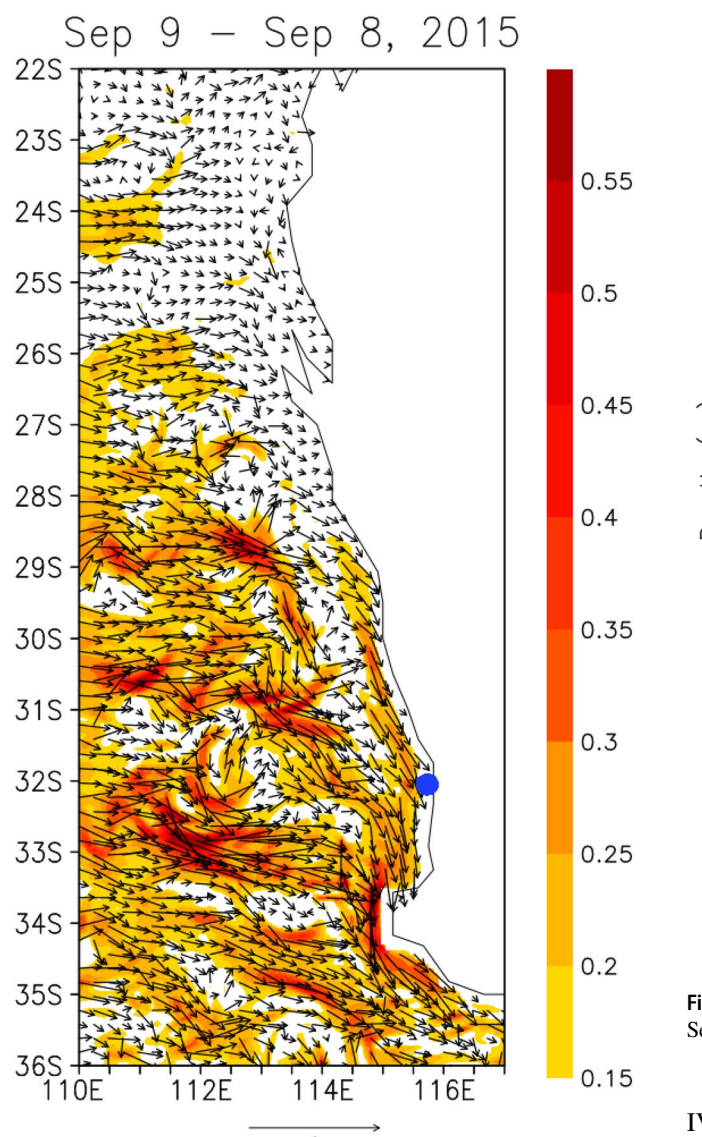


Fig. 5 The difference in surface currents between those on September 8 and September 9, 2015 from the HYCOM reanalysis. Shading indicates the current speed (m/s). The blue dot indicates the location of the Fremantle tide gauge station

of other events, composites of the upper ocean response to ARs off the west coast of Australia are constructed. The compositing method employed in this study is similar to that used in Guo et al. (2020) and Shinoda et al. (2019). Guo et al. (2020) formed composites of moisture and atmospheric circulations around ARs using the global AR data set, in which ARs are objectively detected by the algorithm developed by Guan and Waliser (2015) that is based on characteristics of the integrated water vapor transport (IVT) derived from the ERA-Interim reanalysis (Dee et al. 2011). The AR data set includes key features of ARs at a 6-hourly interval, including the time and location of AR centroid and

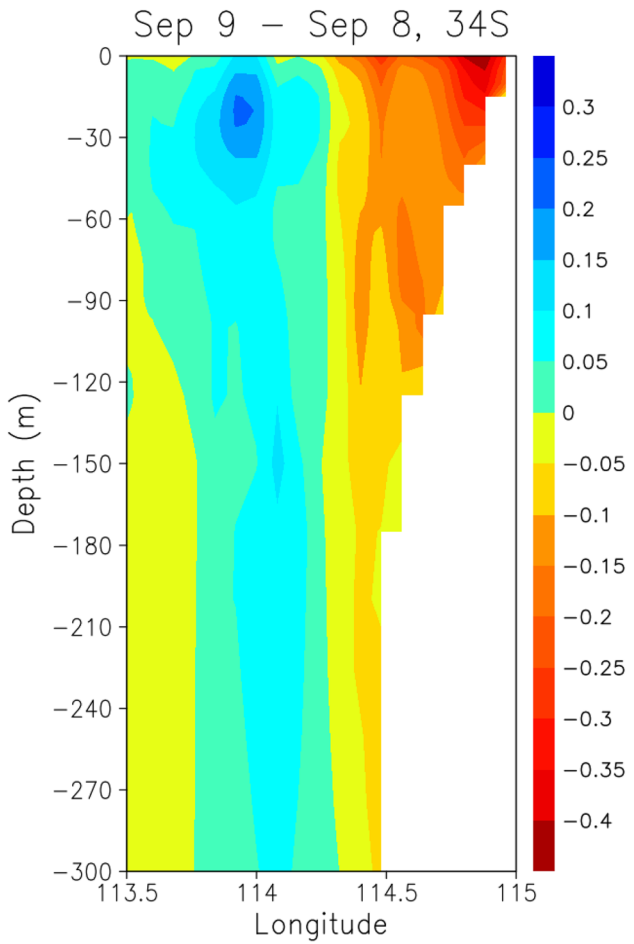


Fig. 6 The difference in meridional velocity along 34° S between September 8 and September 9, 2015 from the HYCOM reanalysis

IVT at the AR center. Here the landfalling AR events along the west coast of Australia are identified as the event for which the AR centroid entered in the area near the coast (35° S-25° S, 112° E-116.5° E) and made landfall. Since the AR is detected at a 6-h interval, ARs could be identified multiple times within a day. In this case, the composites are constructed using the same daily values multiple times. Composites are formed using AR events for the period of 2011–2015, in which 67 landfalling AR events are identified. Landfalling AR events are more frequently observed in austral fall/winter, where 4 events in December-February, 25 events in March-May, 25 events in June-August, and 13 events in September–November are identified. Note that an AR event in this study is defined as the "snapshot" AR, which is different from more traditional definition of AR event that contains all consecutive time points at 6-h intervals during the entire lifetime of an AR.

Figure 8 shows the composite of sea level from the Fremantle tide gauge data. A significant sea level rise associated with ARs, which exceeds 15 cm, is detected in the



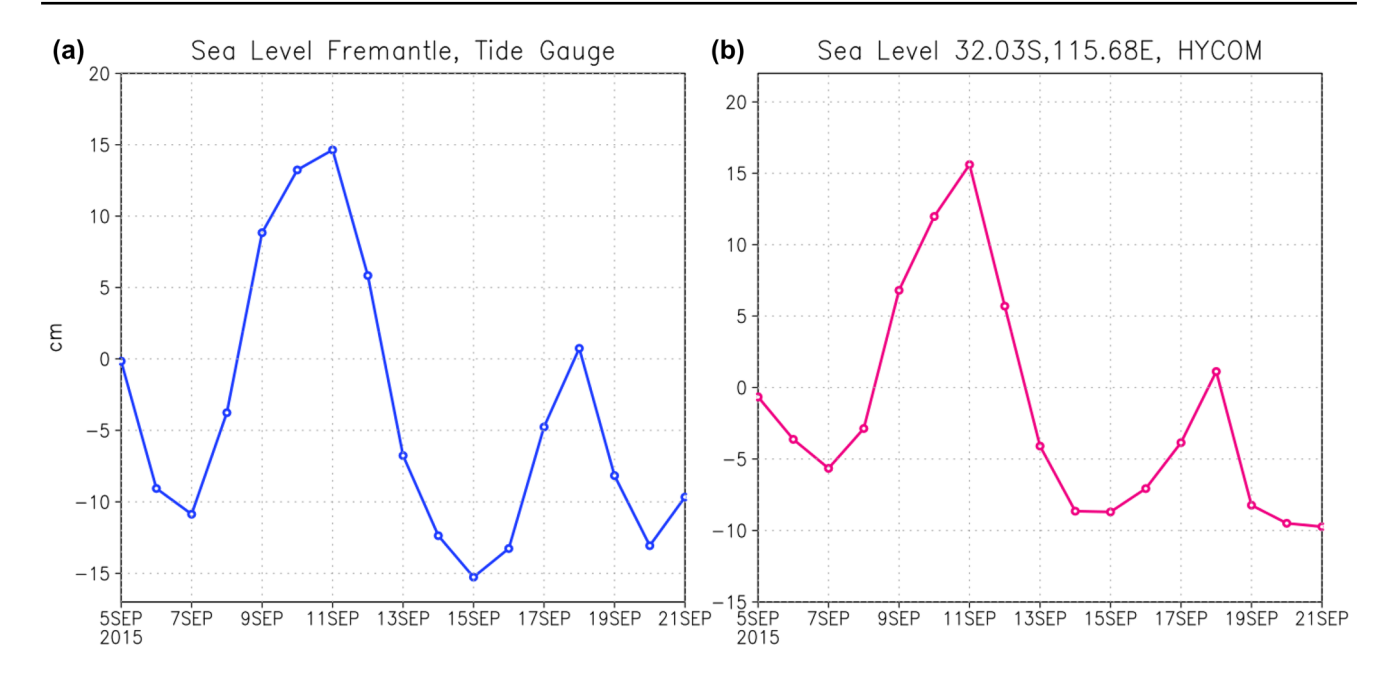


Fig. 7 a Time series of sea level anomaly (cm) from the Fremantle tide gauge data at 32.05° S, 115.72° E. **b** Time series of sea level anomaly from the HYCOM reanalysis at the grid point (32.03° S,

 115.68° E) closest to the Fremantle tide gauge station. Anomalies from both tide gauge and the HYCOM reanalysis are calculated by subtracting the average value of September 2015

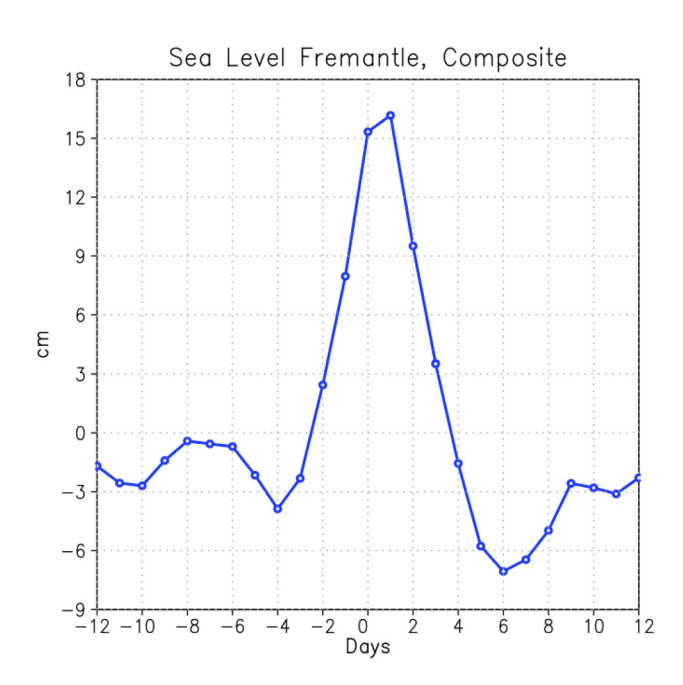


Fig. 8 Composite of sea level (cm) variation at the Fremantle tide gauge station. The composite is formed for AR events that entered in the box in Fig. 9 and made landfall. Day 0 indicates the day when the AR center is located inside of the box in Fig. 9. See text for details of composite calculation

composite. The increase of sea level occurs for 3–4 days before it reaches its maximum, which is consistent with the rapid increase of sea level observed during the event in early

September, 2015 (Fig. 7). The composite map of SSH and surface current variations from the HYCOM reanalysis is shown in Fig. 9. Here the composite variation is defined as the values on Day 0 relative to those on Day – 4 when the increase of SSH begins. The direction of surface currents off the coast in the open ocean area is mostly toward the coast, which is nearly perpendicular to the coastline. The strong surface currents converging to the coast generate the sea level rise in the broad area of the west coast of Australia, which is associated with the acceleration of strong narrow southward currents along the coast.

The vertical structure of the southward current acceleration along the coast is shown in Fig. 10. On Day (-5)before the rapid acceleration occurs, the maximum surface velocity of the LC is about 0.4 m/s, whose core is located around 114.4°E (Fig. 10a). Then the southward currents are accelerated to about 0.6 m/s by Day (0) (Fig. 10b), which is about 50% increase from the velocity before the rapid acceleration associated with the AR landfall. The magnitude of the maximum enhancement, that exceeds 0.3 m/s, is evident right near the coast around 114.7°E (Fig. 10c), which is consistent with the oceanic coastally trapped wave response (a maximum velocity at the coast) and the case study (Fig. 6). However, the location of the maximum velocity of the LC is farther offshore, and thus the enhancement is smaller, which is about 0.2 m/s. Yet this enhancement at the LC core is still comparable to the strength of the mean LC. Note that changes in meridional velocity around the LC core during the enhancement (0.1–0.2 m/s) are statistically significant



since the 95% confidence interval around this area in the composite is about \pm 0.05 m/s.

On Day (-5), the southward velocity right near the coast where the maximum enhancement is found is very weak (close to 0). Then the coastal currents are accelerated to about 0.3 m/s. This acceleration of surface currents and subsequent decay are described in the longitude-time diagram (Fig. 10d), showing that the decay of the currents around the LC core takes much longer than the rapid acceleration associated with the AR landfall. This suggests that the influence of AR-associated surface currents remains after ARs move away from the west coast. The vertical structure of the enhancement (Fig. 10c) is similar to the case study (Fig. 6), in which a significant acceleration extends to about a 200 m depth. The weak acceleration of southward currents starts between Day (-4) and Day (-3) before the AR landfall. This is because the change in wind direction associated with the propagation of anticyclonic circulation ahead of ARs occurs around this period. Note that the spatial scale of ARassociated wind anomalies is generally larger than the scale of the narrow region of water vapor transport.

The strong along-shore currents and the increase of SSH could propagate to remote areas. To examine the influence of these upper ocean fluctuations along the west coast on remote areas, the composite evolution of SSH and surface currents in the entire west and southern coasts of Australia is constructed (Fig. 11). During Day (-1)-Day (+1), the enhancement of southward currents and sea level rise along the west coast are found as in Fig. 9, and these fluctuations are extended to the western portion of southern coast by Day (+1). During Day (+1)-Day (+3), the strong along-shore currents and positive SSH anomalies along the west coast are moved to western and central portions of the southern coast. The SSH and along-shore current fluctuations are then extended to the eastern portion of the southern coast by Day (+5). These anomalous SSH and along-shore currents are further propagated to the Pacific side of the southern coast by Day (+9).

The propagation of SSH along the west coast and southern coast is also detected clearly in the tide gauge data along the coast. Figure 12 shows the composite sea level variation calculated from the tide gauge data from the four stations indicated in Fig. 11 (upper left panel). The time lag of maximum sea level at these stations clearly reveals the propagation from the west coast to the eastern portion of southern coast, which is consistent with the SSH composite from the HYCOM reanalysis. The agreement between the tide gauge data and HYCOM reanalysis confirms that the propagation of SSH and along-shore currents produced by ARs along the west and southern coasts detected by the analysis of HYCOM reanalysis is realistic.

To further quantify the characteristics of the propagation, a Hovmöllor diagram of SSH anomaly along the coast

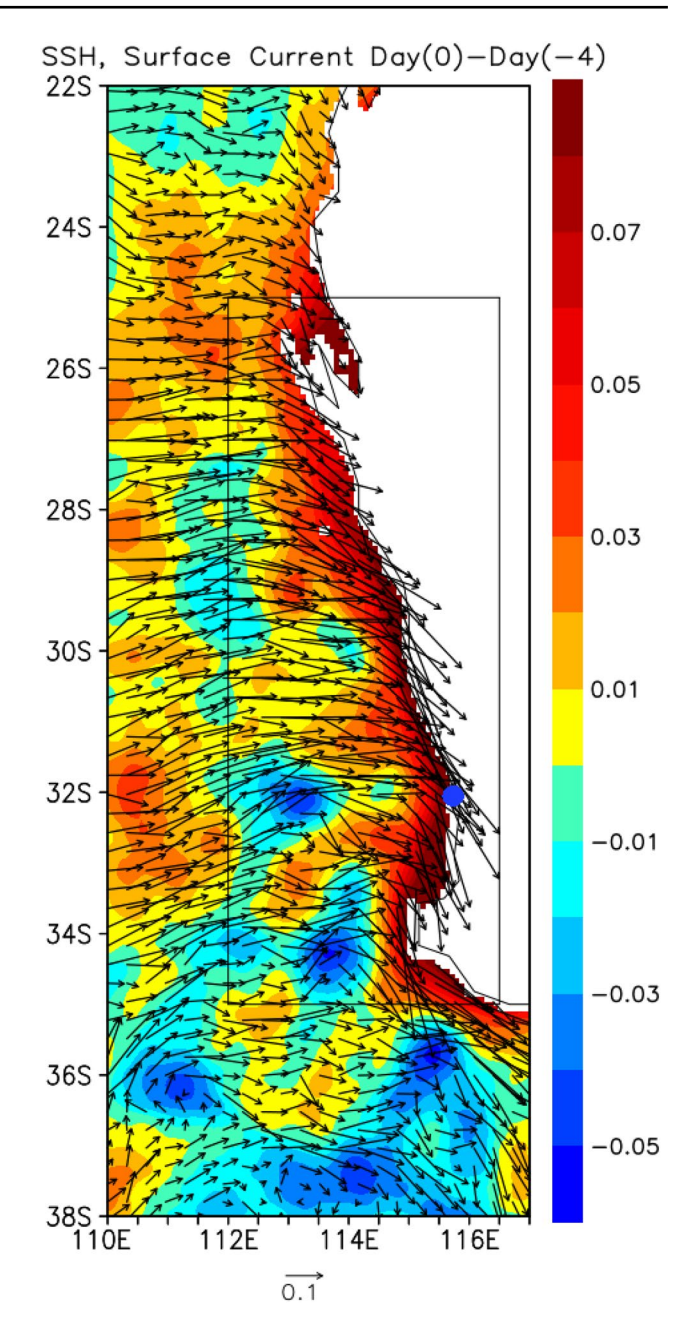


Fig. 9 The difference of composite sea surface height (m: shading) and surface currents (m/s: arrows) between Day 0 and Day -4 from the HYCOM reanalysis. The boxed area is used for identifying the landfalling ARs to form the composite

is constructed (Fig. 13). The average phase speed based on the diagram is about 5.5 m/s, which is much faster than that of free oceanic coastal Kelvin waves but much slower than the speed of the movement of atmospheric disturbance associated with ARs. In addition to Kelvin waves, coastally trapped waves (e.g., Hamon 1962; Adams and Buchwald 1969; Brink 1991) can be generated in the west and southern coasts of Australia because of relatively wide shelf slopes in most areas along the coast. Coastally



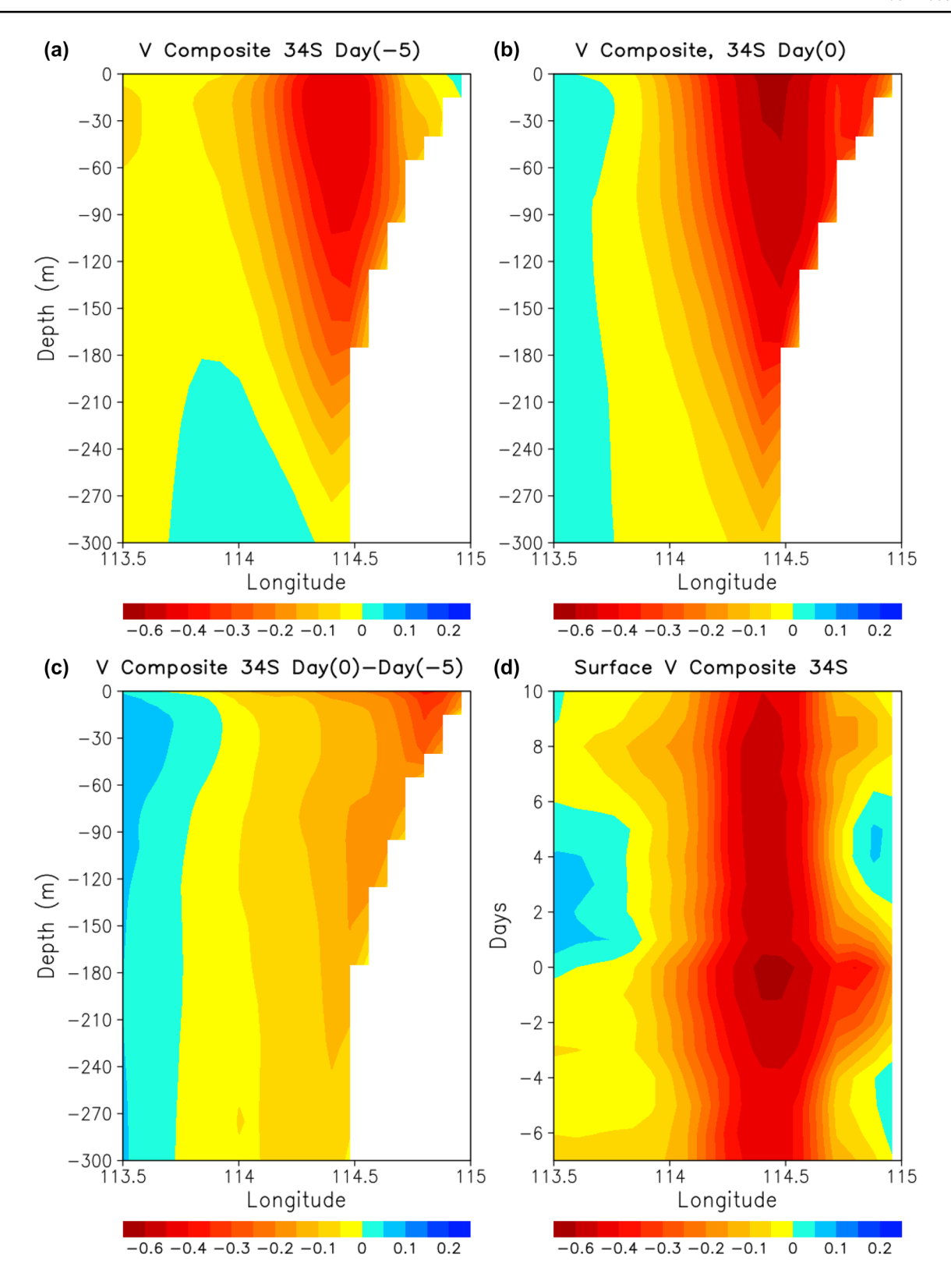


Fig. 10 a The composite meridional velocity (m/s) along 34° S on Day -5. b Same as b except on Day 0. c The difference in meridional velocity between Day 0 and Day -5. d A longitude-time diagram of composite meridional velocity at the surface along 34° S



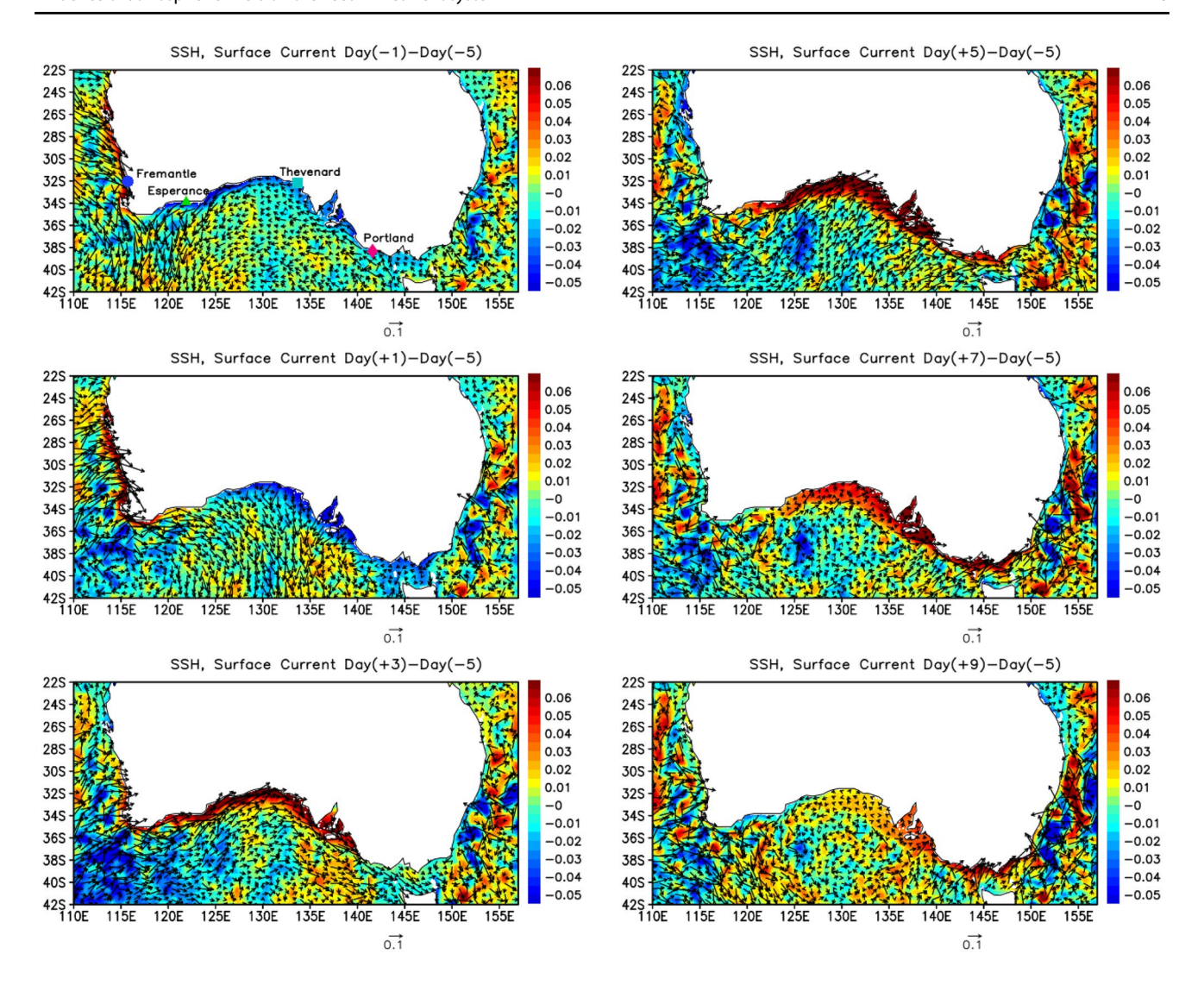


Fig. 11 The difference of composite sea surface height (m: shading) and surface currents (m/s: arrows) between Day - 1 and Day - 5 (upper left), Day+1 and Day - 5 (middle left), Day+3 and Day - 5 (bottom left), Day+5 and Day - 5 (upper right), Day+7 and

Day -5 (middle right), Day +9 and Day -5 (bottom right) from the HYCOM reanalysis. Marks in the upper left panel indicate the locations of tide gauge stations Fremantle (blue circle), Esperance (green triangle), Thevenard (cyan square), and Portland (red diamond)

trapped waves are a hybrid form of wave between internal Kelvin waves and topographic Rossby waves as a result of a sloping bottom and stratification (e.g., Gill and Clark 1974; Wang and Moores 1976; Brink 1991). Previous studies (e.g., Maiwa et al. 2010; Woodham et al. 2013) suggest a relatively wide range of phase speed of coastally trapped waves along Australian coasts (2.5—10 m/s). The barotropic structure of along-shore current enhancement shown in Fig. 10c is consistent with the vertical structure of coastally trapped waves. While the phase speed of the propagation found in the analysis shown in Fig. 13 is within the range of coastally trapped waves, the composite analysis of surface winds suggests a dominant contribution of AR-associated winds along the southern coast in some portions of the propagation. The interpretation of the

phase speed of SSH and along-shore currents is provided in the following.

Figure 14 shows the composite of surface winds on Day (-1), Day (+3), and Day (+5). On Day (+3), the northwesterlies, which accelerated the southward coastal currents along the west coast around Day (-1), move to the Pacific side (Fig. 14, top and middle panels). The spatial pattern of winds on Day (+3) indicates that behind (western side of) the northwesterlies there are southwesterlies in the western part of southern coast, which could generate anomalous eastward currents and sea level rise along the southern coast. The southwesterlies quickly move to the eastern part of southern coast by Day (+5) (Fig. 14, bottom panel).

Such acceleration of coastal currents associated with sea level rise along the southern coast produced by the



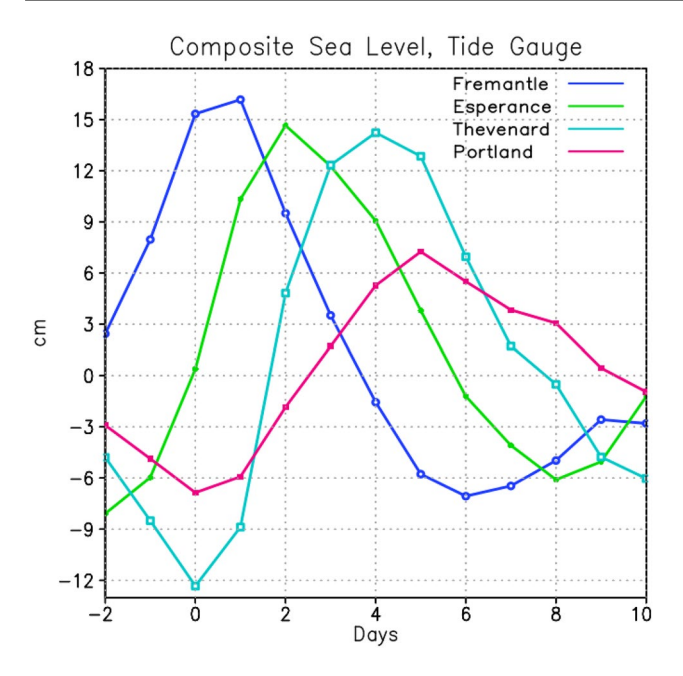
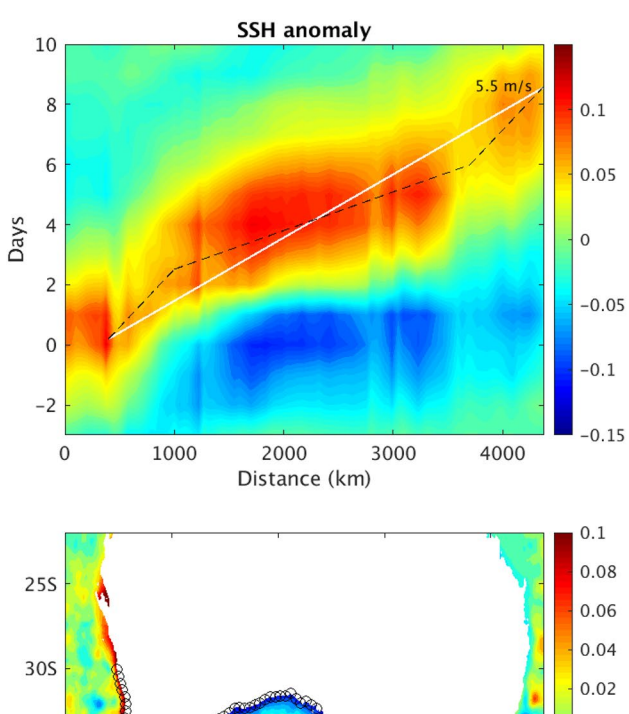


Fig. 12 Composite of sea level (cm) variation at tide gauge stations Fremantle (blue line), Esperance (green line), Thevenard (cyan line), and Portland (red line). See the upper left panel in Fig. 11 for the locations

southwesterlies and their fast eastward movement are evident in Figs. 11 and 13. During Day (-1)-Day (+1), the fluctuation of SSH and along-shore currents along the west coast generated by northweterlies propagate at a relatively slow speed (~3 m/s) to the southern coast, which is consistent with the (oceanic) coastally trapped wave propagation (Fig. 13). These fluctuations quickly move to the eastern portion of southern coast as southwesterlies move eastward (Fig. 11). The phase speed during this period is faster than that during Day (-1)-Day (+1) and consistent with the speed of atmospheric disturbance (Fig. 13). After the southwesterlies move to Pacific side, the SSH and along-shore currents propagate farther to the east again at the slower speed and reach the Pacific side. The propagation speed during this period is consistent with that of coastally trapped wave (Fig. 13).

While the fast propagation speed along the southern coast (9–10 m/s) is still within the range of possible phase speed of coastally trapped waves, it does not agree well with previous observational and modeling studies on coastally trapped waves around this region. For example, Maiwa et al. (2010) indicate that the phase speed of coastally trapped waves along the southern coast between Thevenard and Portland is about 4.5 m/s, which is much slower than the propagation speed found in the analysis here. Although the signal of sea level fluctuation could be a mixture of direct windforced component and oceanic coastally trapped waves, the result suggests that the component forced by local winds is



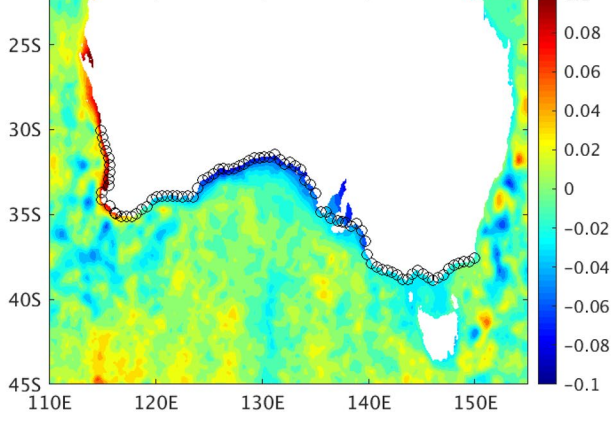


Fig. 13 Upper panel: Hovmoller diagram of composite SSH anomaly (m) along the west and southern coasts of Australia indicated by circles in the lower panel from the HYCOM reanalysis. The horizontal axis indicates the distance of coast line between each station shown by circles in the map (lower panel) and the most northerly location of circles along the west coast $(30.04^{\circ} \text{ S}, 114.88^{\circ} \text{ E})$. The SSH anomaly at each location is calculated by subtracting the time mean of SSH at each location. The solid white line indicates the phase line of 5.5 m/s phase speed. The dashed black line indicates the phase line of 9 m/s (middle part) and 3 m/s (left and right parts) phase speed. The color shading in the lower panel indicates the SSH composite at Day 0 relative to that on Day -5

dominant for the fast propagation along the southern coast. Such modification of wave phase speed by the surface wind forcing has been observed in other regions. For example, the equatorial Kelvin wave speed could be substantially modified by the MJO-induced wind forcing (Shinoda et al. 2008).

In summary, the structure of upper ocean variability along the west coast of Australia associated with ARs derived from the composite analysis is similar to and consistent with that from the case study discussed in the previous section. The composite analysis further demonstrates the propagation of SSH and along-shore currents produced by ARs at the west coast all the way to the Pacific side of southern coast.



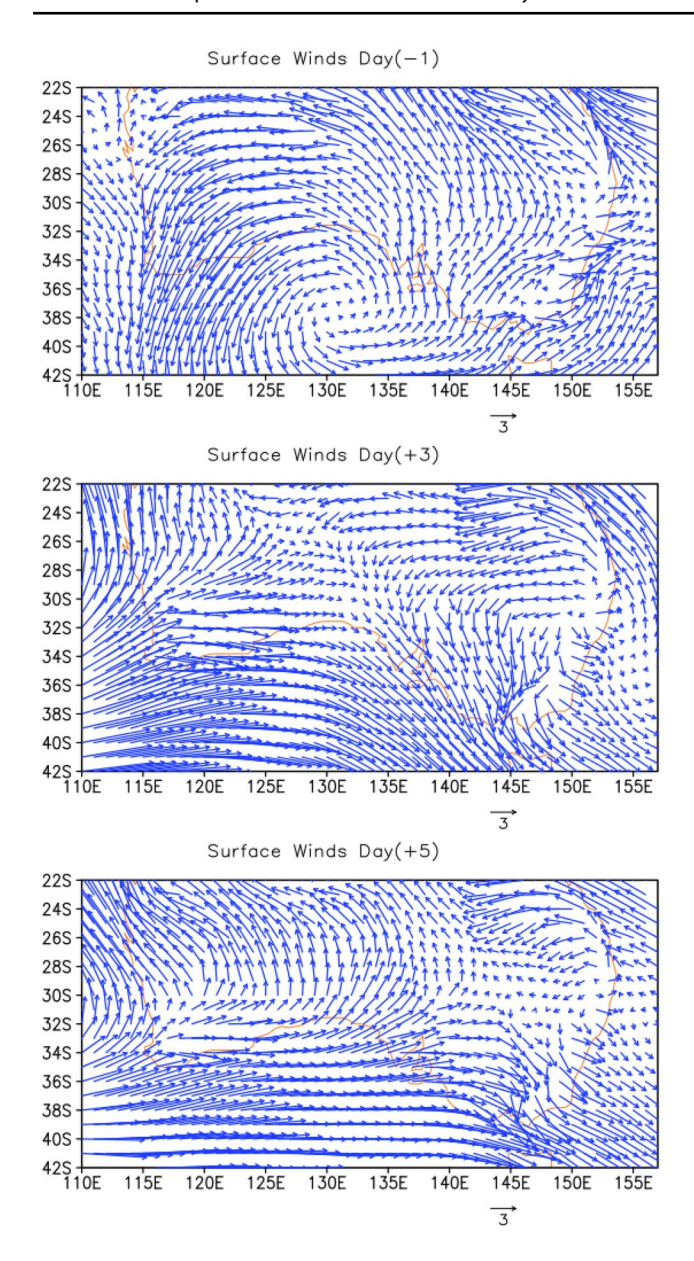


Fig. 14 Composites of surface (10 m height) wind vector (arrows) (m/s) on Day - 1 (top panel) Day + 3 (middle panel), and Day + 5 (bottom panel)

4 Summary and discussion

Ocean variability produced by landfalling ARs along the west coast of Australia and its influence on the Leeuwin Current (LC) system are investigated using the high-resolution (0.08°) ocean reanalysis and tide gauge data. ARs in the southeast Indian Ocean often make landfall along the west coast of Australia. A case study of one of the typical landfalling AR events indicate that AR-associated surface northwesterly winds generate strong surface currents toward the coastline. During the landfalling of AR, the on-shore surface currents flow against the coast, resulting in generating

strong anomalous southward currents along the coast. The southward currents are associated with prominent sea level rise in the broad areas along the west coast of Australia.

The composite evolution of ocean variability produced by landfalling AR events is constructed. Major features found in the case study are all evident in the composite structure and evolution of ocean variability associated with ARs. Hence these analyses indicate that typical landfalling ARs in the southeast Indian Ocean generate strong poleward coastal currents and sea level rise along the west coast of Australia, which largely enhances the southward flowing LC. While the maximum of AR-induced coastal currents occurs right near the coast, the core of the LC is located farther offshore about 30–50 km west of the coastline. Yet the enhancement of southward currents at the LC core, which is about 50% of the LC strength before the acceleration, is comparable to the strength of the LC itself.

The analysis further demonstrates that the fluctuation of SSH and coastal current along the west coast generated by ARs propagates along the southern coast of Australia all the way to the southeast coast (Pacific side). This propagation is evident in both the HYCOM reanalysis and the tide gauge data at four stations along the west and southern coasts. The average phase speed of the propagation is about 5.5 m/s, which is much slower than the movement of atmospheric disturbance associated with ARs but much faster than oceanic free Kelvin waves. However, the phase speed largely depends on the location. For the period of propagation from the west coast to southwest coast, the phase speed is consistent with oceanic coastally trapped waves. However, the phase speed along the southern coast is faster and consistent with the speed of atmospheric disturbance. This is because the southwesterlies associated with ARs, which are located west side of northwesterlies, generate eastward along-shore currents and sea level rise along the southern coast which moves with the atmospheric disturbance. After the southwesterlies move to the Pacific side, SSH and along-shore currents further propagate in a slower speed which is consistent with the phase speed of oceanic coastally trapped wave.

Because of the changes in coastline direction during the propagation, SSH and coastal currents initially propagated by oceanic coastally trapped waves are effectively forced by the AR-associated winds along the southern coast. As a result, large areas of SSH and coastal currents along the Australian coasts are affected by each AR event. The LC flows from west coast of Australia, and enters southern coast which farther extends as far as southeast coast around Tasmania. The analyses suggest that AR-induced coastal currents could influence almost the entire pathway of the LC south of around 25° S.

Although the time scale of ocean response to atmospheric disturbance associated with ARs is only several days, it is



possible that frequent occurrence of AR may have a significant impact on the longer time scale SST and upper ocean temperature variation. However, the processes that control SST and upper ocean temperature in this region may be quite complex. For example, SSTs are influenced by the LC which brings warm waters from the tropics, while large latent heat flux associated with AR-associated winds may generate cooling. Unlike eastern boundaries in other ocean basins, relatively warm SSTs are maintained in this region by the poleward flowing LC and thus both mean and variability of latent heat flux are large (e.g., Feng et al. 2008; Feng and Shinoda 2019). Hence the occasional strong winds associated with ARs could generate large SST cooling, and thus the net effect of ARs on SSTs could be determined by complex oceanic processes which include large evaporative cooling and horizontal advection of warm waters.

Processes on AR-induced SST changes are further complicated by the difference in ocean response between the west and southern coasts because of the different direction of the coastlines. Strong northeasterlies during the AR landfall generate upwelling along the southern coast and weak westward currents that tends to reduce the LC at least during the initial response (Figs. 11, 13, 14). Such strong upwelling may generate significant cooling along the southern coast. The initial response along the west coast is quite different, where the primary response is the enhancement of the LC and strong downwelling by the northwesterlies. Further thorough analyses, that include upper ocean heat budget associated with ARs, are required to fully establish the overall influence of AR-induced oceanic processes on SST and regional climate, which is one of our on-going and future studies.

Acknowledgements Grants of computer time for the HYCOM reanalysis were provided by the Department of Defense (DoD) High Performance Computing Modernization Program, and the reanalysis was performed at the Navy DoD Supercomputing Resources Center, Stennis Space Center, MS. Computing resources were also provided by the Climate Simulation Laboratory at NCAR's Computational and Information Systems Laboratory, sponsored by the National Science Foundation, and the HPC systems at the Texas A&M University, College Station and Corpus Christi. The tide gauge data are obtained from the University of Hawaii Sea Level Center. This research is supported by NSF grants AGS-1347132 and OCE-1658218, and NASA grants NNX17AH25G and NNX17AI63G. TS is also supported by NOAA grants NA15OAR431074 and NA17OAR4310256. Constructive comments by a reviewer George Kiladis and other two anonymous reviewers are gratefully acknowledged.

References

- Adams JK, Buchwald VT (1969) The generation of continental shelf waves. J Fluid Mech 35:815–826
- Andrews JC (1977) Eddy structure and the West Australian Current. Deep-Sea Res 24:1133–1148
- $\underline{\underline{\mathscr{D}}}$ Springer

- Bao J-W, Michelson SA, Neiman PJ, Ralph FM, Wilczak JM (2006) Interpretation of enhanced integrated water-vapor bands associated with extratropical cyclones: their formation and connection to tropical moisture. Mon Wea Rev 134:1063–1080
- Batteen ML, Butler L, Bayler EJ (1992) A numerical study of windand thermal-forcing effects on the ocean circulation off western Australia. J Phys Oceanogr 22:1406–1433
- Batteen ML, Butler CL (1998) Modeling studies of the Leeuwin Current off western and southern Australia. J Phys Oceanogr 28:2199–2221
- Bleck R (2002) An oceanic general circulation model framed in hybrid isopycnic-Cartesian coordinates. Ocean Model 4:55–88
- Brink KH (1991) Coastal-trapped waves and wind-driven currents over the continental shelf. Annu Rev Fluid Mech 23:389–412
- Church JA, Cresswell GR, Godfrey JS (1989) The Leeuwin Current. In: Neshyba SJ, Moors CNK, Smith RL, Barber RT (eds) Pole-wardflows along eastern ocean boundaries. Coastal and estuarine studies, vol 34. Springer, New York, pp 230–254
- Cresswell GR, Golding TJ (1980) Observations of a south-flowing current in the southeastern Indian Ocean. Deep Sea Res 27:449-466
- Cummings JA, Smedstad OM (2013) Variational data assimilation for the global ocean. In: Park SK, Xu L (eds) Data assimilation for atmospheric, oceanic and hydrologic applications. Springer, Berlin, pp 303–343
- Dee DP et al (2011) The ERA-Interim reanalysis: configuration and performance of the data assimilation system. Q J R Meteorol Soc 137:553–597
- Dettinger MD (2011) Climate change, atmospheric rivers and floods in California—a multimodel analysis of storm frequency and magnitude changes. J Am Water Resour Assoc 47(3):514–523
- Doyle JD, Amerault C, Reynolds CA, Reinecke PA (2014) Initial condition sensitivity and predictability of a severe extratropical cyclone using a moist adjoint. Mon Wea Rev 142:320–342
- Feng M, McPhaden MJ, Xie S-P, Hafner J (2013) La Niña forces unprecedented Leeuwin Current warming in 2011. Sci Rep 3:1–9. https://doi.org/10.1038/srep01277
- Feng M, Meyers G, Pearce A, Wijffels S (2003) Annual and interannual variations of the Leeuwin Current at 32° S. J Geophys Res 108:3355. https://doi.org/10.1029/2002JC001763
- Feng M, Wijffels S, Godfrey S, Meyers G (2005) Do eddies play a role in the momentum balance of the Leeuwin Current? J Phys Oceanogr 35:964–975
- Feng M, Biastoch A, Boning C, Caputi N, Meyers G (2008) Seasonal and interannual variations of upper ocean heat balance off the west coast of Australia. J Geophys Res 113:C12025
- Feng X, Shinoda T (2019) Air—sea heat flux variability in the southeast Indian Ocean and its relation with Ningaloo Niño. Front Mar Sci. https://doi.org/10.3389/fmars.2019.00266
- Furue R, Guerreiro K, Phillips HE, McCreary JP, Bindoff NL (2017) On the Leeuwin Current system and its linkage to zonal flows in the South Indian Ocean as inferred from a gridded hydrography. J Phys Oceanogr 47(3):583–602
- Gill AE, Clarke AJ (1974) Wind-induced upwelling, coastal currents and sea-level changes. Deep-Sea Res 21:325–345
- Guo G, Shinoda T, Guan B, Waliser DE, Chang EKM (2020) Statistical relationship between atmospheric rivers, extratropical cyclones, and anticyclones. J Clim (revised)
- Guan B, Molotch NP, Waliser DE, Fetzer EJ, Neiman PJ (2010) Extreme snowfall events linked to atmospheric rivers and surface air temperature via satellite measurements. Geophys Res Lett 37:L20401. https://doi.org/10.1029/2010GL044696
- Guan B, Molotch NP, Waliser DE, Fetzer EJ, Neiman PJ (2013) The 2010/2011 snow season in California's Sierra Nevada: role of atmospheric rivers and modes of large-scale variability. Water Resour Res 49:6731–6743. https://doi.org/10.1002/wrcr.20537

- Guan B, Waliser DE (2015) Detection of atmospheric rivers: evaluation and application of an algorithm for global studies. J Geophys Res-Atmos 120:1251412535. https://doi.org/10.1002/2015JD024257
- Guan B, Waliser DE, Ralph FM (2018) An inter-comparison between reanalysis and dropsonde observations of the total water vapor transport in individual atmospheric rivers. J Hydrometeorol 19:321–337. https://doi.org/10.1175/JHM-D-17-0114.1
- Hamon BV (1962) The spectrums of mean sea level at Sydney, Coffs Harbour and Lord Howe Island. J Geophys Res 67:5147–5155
- Helber et al (2013) Validation test report for the improved synthetic ocean profile (ISOP) system, Part I: Synthetic profile methods and algorithm NRL memorandum report NRL/MR/7320-13-9364, pp 1–66
- Hirota N, Takayabu YN, Kato M, Akane S (2016) Roles of an atmospheric river and a cutoff low in the extreme precipitation event in Hiroshima on 19 August 2014. Mon Wea Rev 144:1145–1160
- Kim H-M, Alexander MA (2015) ENSO's modulation of water vapor transport over the Pacific–North American region. J Clim 28:3846–3856
- Kim H-M, Zhou Y, Alexander MA (2017) Changes in atmospheric rivers and moisture transport over the Northeast Pacific and western North America in response to ENSO diversity. Clim Dyn. https://doi.org/10.1007/s00382-017-3598-9
- Leung LR, Qian Y (2009) Atmospheric rivers induced heavy precipitation and flooding in the Western U.S. simulated by the WRF regional climate model. Geophys Res Lett 36:L03820. https://doi.org/10.1029/2008GL036445
- Maiwa K, Masumoto Y, Yamagata T (2010) Characteristics of coastal trapped waves along the southern and eastern coasts of Australia. J Oceanogr 66:243–258
- Metzger EJ et al (2014) US Navy operational global ocean and Arctic ice prediction systems, special issue on navy operational models. Oceanography 27(3):32–43. https://doi.org/10.5670/oceanog.2014.66
- Mundhenk BD, Barnes E, Maloney E (2016) All-season climatology and variability of atmospheric river frequencies over the North Pacific. J Clim 29:4885–4903
- Neiman PJ, Ralph FM, Wick GA, Lundquist J, Dettinger MD (2008) Meteorological characteristics and overland precipitation impacts of atmospheric rivers affecting the West Coast of North America based on eight years of SSM/I satellite observations. J Hydrometeorol 9:22–47. https://doi.org/10.1175/2007JHM855.1
- Newell RE, Zhu Y (1994) Atmospheric rivers and bombs. Geophys Res Lett 21:1999–2002
- Pearce AF, Griffiths RW (1991) The mesoscale structure of the Leeuwin Current: a comparison of laboratory model and satellite images. J Geophys Res 96:16730–16757

- Ralph FM, Neiman PJ, Wick GA (2004) Satellite and CALJET aircraft observations of atmospheric rivers over the eastern North-Pacific Ocean during the winter of 1997/98. Mon Wea Rev 132:1721–2174
- Ralph FM et al (2006) Flooding on California's Russian River. Role of atmospheric rivers. Geophys Res Lett 33:L13801. https://doi. org/10.1029/2006GL026689
- Reynolds CA, Doyle JD, Ralph MF, Demirdian R (2019) Adjoint sensitivity of North Pacific atmospheric river forecasts. Mon Wea Rev. https://doi.org/10.1175/MWR-D-18-0347.1
- Saha S et al (2010) The NCEP climate forecast system reanalysis. Bull Am Meteorol Soc 91:1015. https://doi.org/10.1175/2010BAMS30
- Shinoda T, Roundy P, Kiladis G (2008) Variability of intraseasonal Kelvin waves in the equatorial Pacific Ocean. J Phys Oceanogr 38:921–944
- Shinoda T, Zamudio L, Guo Y, Metzger EJ, Fairall C (2019) Ocean variability and air-sea fluxes produced by atmospheric rivers. Sci Rep. https://doi.org/10.1038/s41598-019-38562-2
- Thoppil PG, Metzger EJ, Hurlburt HE, Smedstad OM, Ichikawa H (2016) The current system east of the Ryukyu Islands as revealed by a global ocean reanalysis. Prog Oceanogr 141:239–258
- Yu Z et al (2015) Seasonal cycle of volume transport through Kerama Gap revealed by a 20-year global hybrid coordinate ocean model reanalysis. Ocean Model 96:203–213
- Waliser DE, Guan B (2017) Extreme winds and precipitation during landfall of atmospheric rivers. Nat Geosci. https://doi. org/10.1038/NGEO2894
- Wang D-P, Mooers CNK (1976) Coastal trapped waves in a continuously stratified ocean. J Phys Oceanogr 6:853–863
- Woodham R, Brassington GB, Robertson R, Alves O (2013) Propagation characteristics of coastally trapped waves on the Australian continental shelf. J Geophys Res Oceans 118:4461–4473
- Zhang L, Han W (2018) Impact of Ningaloo Niño on tropical pacific and an interbasin coupling mechanism. Geophys Res Lett. https://doi.org/10.1029/2018GL078579
- Zhu Y, Newell RE (1998) A proposed algorithm for moisture fluxes from atmospheric rivers. Mon Wea Rev 126:725–735

Publisher's Note Springer Nature remains neutral with regard to jurisdictional claims in published maps and institutional affiliations.

